AGU PUBLICATIONS

JGR

Journal of Geophysical Research: Space Physics

TECHNICAL REPORTS: DATA

10.1002/2016JA023342

This article is a companion to *Redmon et al.* [2017] doi:10.1002/2016JA023339.

Key Points:
- New DMSP magnetometer and auroral boundary data set
- Recomputed magnetic perturbations and calculated field-aligned currents
- Estimated FAC density in dynamic auroral boundary coordinates shows dawn-dusk asymmetry

Supporting Information:
- Supporting Information S1

Correspondence to:
L. M. Kilcommons,
liam.kilcommons@colorado.edu

Citation:
Kilcommons, L. M., R. J. Redmon, and D. J. Knipp (2017), A new DMSP magnetometer and auroral boundary data set and estimates of field-aligned currents in dynamic auroral boundary coordinates, *J. Geophys. Res. Space Physics*, *122*, 9068–9079, doi:10.1002/2016JA023342.

Received 15 AUG 2016
Accepted 1 APR 2017
Accepted article online 10 APR 2017
Published online 10 AUG 2017

A new DMSP magnetometer and auroral boundary data set and estimates of field-aligned currents in dynamic auroral boundary coordinates

Liam M. Kilcommons[1], Robert J. Redmon[2], and Delores J. Knipp[1,3]

[1]Aerospace Engineering Sciences, University of Colorado Boulder, Boulder, Colorado, USA, [2]National Center for Environmental Information (NCEI), National Oceanic and Atmospheric Administration (NOAA), Boulder, Colorado, USA, [3]High Altitude Observatory, National Center for Atmospheric Research, Boulder, Colorado, USA

Abstract We have developed a method for reprocessing the multidecadal, multispacecraft Defense Meteorological Satellite Program Special Sensor Magnetometer (DMSP SSM) data set and have applied it to 15 spacecraft years of data (DMSP Flight 16–18, 2010–2014). This Level-2 data set improves on other available SSM data sets with recalculated spacecraft locations and magnetic perturbations, artifact signal removal, representations of the observations in geomagnetic coordinates, and in situ auroral boundaries. Spacecraft locations have been recalculated using ground-tracking information. Magnetic perturbations (measured field minus modeled main field) are recomputed. The updated locations ensure the appropriate model field is used. We characterize and remove a slow-varying signal in the magnetic field measurements. This signal is a combination of ring current and measurement artifacts. A final artifact remains after processing: step discontinuities in the baseline caused by activation/deactivation of spacecraft electronics. Using coincident data from the DMSP precipitating electrons and ions instrument (SSJ4/5), we detect the in situ auroral boundaries with an improvement to the Redmon et al. (2010) algorithm. We embed the location of the aurora and an accompanying figure of merit in the Level-2 SSM data product. Finally, we demonstrate the potential of this new data set by estimating field-aligned current (FAC) density using the Minimum Variance Analysis technique. The FAC estimates are then expressed in dynamic auroral boundary coordinates using the SSJ-derived boundaries, demonstrating a dawn-dusk asymmetry in average FAC location relative to the equatorward edge of the aurora. The new SSM data set is now available in several public repositories.

1. Introduction

The United States Air Force Defense Meteorological Satellite Program (USAF DMSP) has flown earth-observing spacecraft since 1962 [*Hall*, 2001]. The most recent series of DMSP, Block 5D-3, orbits at approximately 850 km geodetic altitude in a near-circular, Sun-synchronous orbit (inclination 98.8°) with an orbital period of 101 min.

As part of a suite of space environment sensors, several DMSP spacecraft have carried a triaxial fluxgate magnetometer. The first magnetometer-equipped DMSP was Flight 7 (F07) launched on 18 November 1983, but the instrument did not become part of the standard DMSP payload until F12 (launched in early 1994). The DMSP Special Sensor Magnetometer (SSM) instrument was designed to be accurate enough to measure the magnetic signatures of field-aligned currents (FAC), also known as Birkeland or region 1 and region 2 currents. An additional goal was to measure the slow changes in the portion of the Earth's field created by the dynamo effect of the liquid outer core (the secular variation). Originally, the SSM instrument was mounted on the spacecraft body. However, this close proximity to currents from spacecraft electronics produced undesired signals in the magnetic field measurements. Beginning with DMSP F15, launched in 1999, the SSMs were mounted on the end of a telescoping boom, which more effectively isolated the sensor from spacecraft magnetic noise. Even so, some nuisance signals remain, and this report documents our efforts and techniques to isolate only the signal due to ionospheric (primarily field-aligned) currents.

We also use the reprocessed data from the DMSP Special Sensor J (SSJ4 and SSJ5) described in the companion paper, *Redmon et al.* [2017], which senses precipitating auroral ions and electrons between 30 eV and 30 keV. We apply an algorithm based on that of *Redmon et al.* [2010] to automatically identify when the spacecraft is in the aurora as evidenced by the 1–30 keV electron precipitation. We associate each magnetic field measurement with the particle precipitation environment (polar cap, aurora, or equatorward of the aurora) in which it was

made, providing valuable geophysical context. More details about SSJ4 can be found in *Hardy* [1984]. Both SSJ4 and SSJ5 are described the companion paper [*Redmon et al*., 2017].

In section 2, we describe the magnetometer instrument and its measurements in the Level-1 data format. Section 3 describes our process for removing various undesired signals, culminating in isolating the magnetic perturbations due to FACs. Sections 4 and 5 describe methods for estimating the in situ auroral boundary locations from SSJ electron precipitation, and the FAC density from the SSM magnetic perturbations, respectively. In section 6, we compare the location of region-2 field-aligned currents with the equatorward electron precipitation auroral boundary using nine spacecraft years of combined SSM and SSJ data. In section 7 we provide a concise summary.

2. Instrument and Data Format

The SSM instrument is a triaxial fluxgate magnetometer and consists of three separate cores, each of which is mutually perpendicular to the others. Each core measures one component of the magnetic field vector in a range of ±63,553 nT with an accuracy of 2 nT [*Rich et al*., 2007]. The magnetometer is mounted on the end of a 5 m telescopic boom which deploys after launch. The magnetometer instrument's axes are aligned on the ground to be within 0.05° of the spacecraft body reference frame. The coordinate frame for SSM reflects the older body-mounted orientation with *X*: geodetic downward, *Y*: horizontal and along the spacecraft track, positive in the velocity direction, and *Z*: horizontal and perpendicular to the spacecraft track, with positive to the right of the velocity direction (completing the right-handed coordinate frame). The spacecraft attitude is maintained for the optical instruments, keeping the spacecraft vertical direction within 0.01° of geodetic vertical [*Rich et al*., 2007].

Miller and Sexton [2001] detail the on-orbit calibration of SSM, which models the true field as a linear function of the measured field:

$$\mathbf{B}_{\mathrm{True}} = \mathbf{O}\cdot\mathbf{B}_{\mathrm{Measured}} + \mathbf{S} \tag{1}$$

where **O** is a 3 × 3 matrix and **S** is a 1 × 3 vector. The diagonal elements of **O** quantify the scaling factor between measured value and true magnetic field for a particular vector component. The off-diagonal elements of **O** represent the amount of bleedthrough in signal between each possible pair of the three cores (due to imperfections in orthogonality). **S** is a scalar offset for each core which quantifies the remnant magnetization in the core and the induced field of the spacecraft. Early in the mission of each magnetometer-equipped DMSP spacecraft this model is least squares fit against the International Geomagnetic Reference Field (IGRF) (See IGRF description in *Maus et al*. [2005] and *Finlay et al*. [2010] and calibration description in *Miller and Sexton* [2001]) to create the on-orbit calibration. SSM is not maneuver calibrated on orbit as is common for dedicated magnetometry missions. The SSM data we use in our reprocessing are hosted by National Oceanic and Atmospheric Administration (NOAA) National Centers for Environmental Information (NCEI) in Boulder. The data are provided in ASCII format historically know as MFR. The SSM instrument has a 12 Hz sampling rate and uses a 6 Hz, 20 dB/decade low-pass antialiasing filter to reduce spacecraft contamination [*Chornay*, 1987]. The MFR files contain the averages of these samples at a cadence of approximately 1 s. The full sampling rate data together with housekeeping data is telemetered down, but only the averages were available for this project. Although most measurements are exactly 1 s averages, occasional "staggered" measurements occur, where one measurement follows after the previous in as little as 0.1 s, with the measurement after that delayed up to 1.9 s. Staggered measurements occur for less than 10% of data points. This data feature has been preserved in our Level-2 files.

The locations in MFR files are predictions made using Two Line Element records and uploaded to the spacecraft up to days in advance. These predicted positions often disagree with those computed by spacecraft tracking centers on the ground [*Redmon et al*., 2017]. Accurate spacecraft locations are very important for spacecraft magnetometer data sets because the main field can change by the same order of magnitude (~60 nT), between one observation and the next, as the field due to weak-to-moderate ionospheric currents (see Figure 1c). We reprocess the spacecraft locations for the SSM data set to ensure consistent quality of the ephemerides. A detailed discussion of this process is available in the companion paper [*Redmon et al*., 2017].

At this point, the ephemeris processing for our magnetometer data set extends from that described by *Redmon et al*. [2017]. We add spacecraft locations in Modified Magnetic Apex (henceforth, simply Apex)

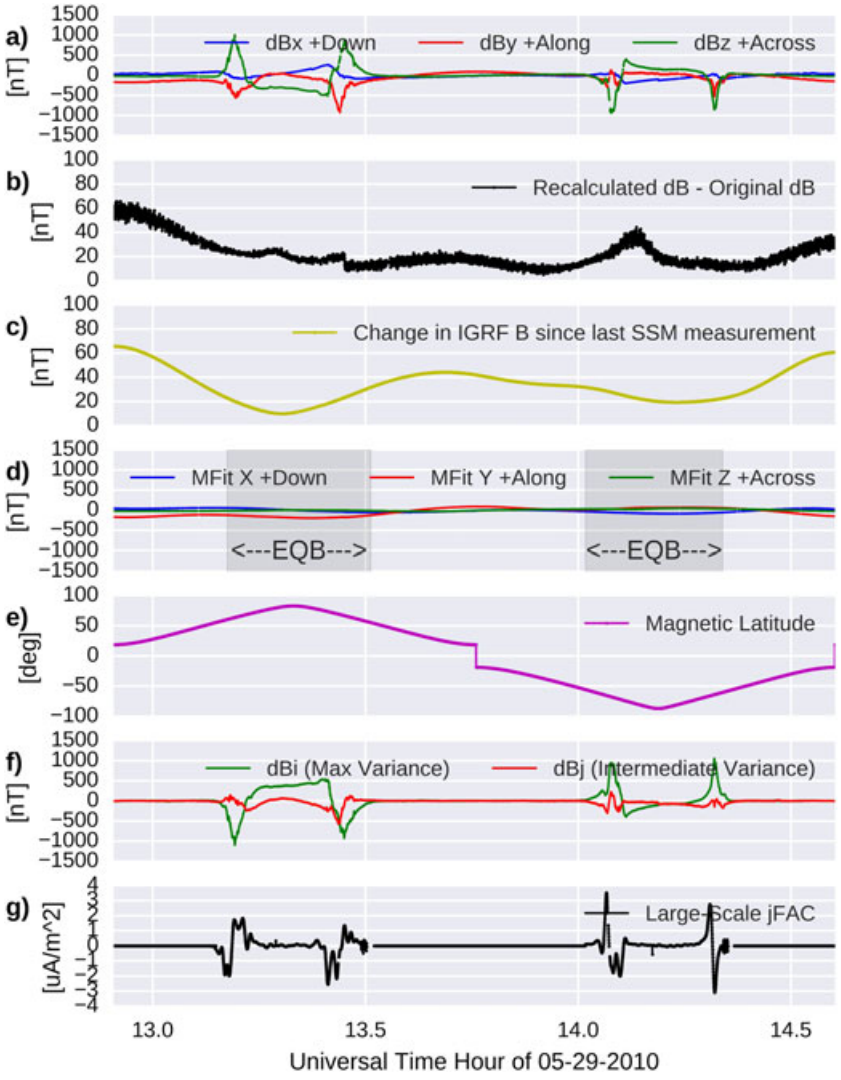

Figure 1. Effect of recomputing perturbations. (a) The magnetic perturbations using the more accurate recomputed ephemeris in the spacecraft coordinate (*XYZ*) frame. (b) The magnitude of the vector difference $|\delta\mathbf{B}_{\text{new}} - \delta\mathbf{B}_{\text{old}}|$ between the newly calculated magnetic perturbations and those in the original MFR files. (c) The change in the IGRF main field from one SSM sample location to the next (as magnitude of vector difference $|\mathbf{B}_{\text{IGRF}}(t+1) - \mathbf{B}_{\text{IGRF}}(t)|$). The difference between our recomputed and the operational perturbations is generally comparable to the change in the main field over the 7 km between SSM measurements, indicating the original ephemeris for these later spacecraft are reasonably good (see supporting information for a direct comparison). (d) The polynomials fit to each magnetometer axes' baselines using only measurements outside the grey shaded auroral/polar cap region. (e) The spacecraft's Apex magnetic latitude for reference. (g and h) The magnetic perturbations rotated from *XYZ* into the *i*, *j*, *k* basis from the Minimum Variance Analysis (MVA) [*Sonnerup and Scheible*, 1998], and the resulting FAC density estimates from equation (4) (see also section 5).

[*Richmond*, 1995]. Since magnetic perturbations are vectors, we also re-express each SSM magnetic perturbation in several alternate bases. In addition to the original spacecraft-centered (*XYZ*), we include geographic east, north, up (GEO ENU), and the Apex "d-basis", which has nominally magnetic eastward (*d1*), magnetic equatorward (*d2*), and main field-aligned (*d3*) components.

To determine the *XYZ* to GEO ENU transformation, we first estimate the spacecraft velocity direction from the geographic ephemerides. We use a technique based on the spherical triangle formed by two adjacent observations and the north magnetic pole (see supporting information Figure S1). With the along-track direction determined, we assume the spacecraft vertical to be parallel to the geographic radial direction (an approximation for tractability, since the spacecraft vertical (*Z* axis) is in fact parallel to geodetic vertical [*Rich et al.*, 2007]) and then complete the right-handed basis set.

The Apex system provides basis vectors for representing vector quantities relative to the geomagnetic main field direction (as represented by the IGRF, 11th Generation [*Finlay et al*., 2010]), which is desirable for physical interpretation of the measurements (e.g., calculating currents or potentials). Although published in 2010, the 11th Generation IGRF provides coefficients for the secular variation through 2015, enabling main field estimates for the dates of all observations used herein. The Apex coordinate system is also used in models (e.g., the Thermosphere Ionosphere Electrodynamics General Circulation Model [*Richmond et al*., 1992]), data assimilation routines (e.g. versions of the Assimilative Mapping of Ionospheric Electrodynamics [*Richmond*, 1992; *Matsuo et al*., 2015], and space-based data comparisons [*Knipp et al*., 2014, 2015], making the new SSM data more compatible for comparison and assimilation.

The Apex expression of the magnetic perturbation vectors requires compatible spacecraft locations. Beginning from the GEO locations, we find the Apex DMSP locations with a reference altitude (h_r) of 110 km. Beginning from the GEO ENU magnetic perturbations, we then transform the perturbations into the magnetic field-aligned Apex "d" basis.

3. Data Processing

This section describes the process for creating the NASA Common Data Format (CDF) [*Mathews and Towheed*, 1995] files which make up the new data set. In section 3.1 we describe the process for estimating the magnetic perturbations due to ionospheric current systems. Sections 3.2 and 3.3 describe our techniques for removing remaining nuisance signals. We discuss uncertainty in the measurements in section 3.4 and finally outline data access in section 3.5.

3.1. Magnetic Perturbations

Although all of the necessary information for using the DMSP SSM data for other uses is preserved in our Level-2 data set, the primary target of our processing is to provide information about the magnetic fields induced by field-aligned currents in the vicinity of the spacecraft. Typically such fields have a magnitude of the order of hundreds of nanotesla, with storm time values up to about 3000 nT [*Knipp et al*., 2014, 2015]. Since the strength of the Earth's main magnetic field is around 50,000 nT, the FAC-induced perturbations can be difficult to differentiate from contributions from Earth's magnetic field and from magnetic fields associated with the spacecraft itself. In addition, all spacecraft locations have some uncertainty which can cause error in magnetic perturbations because the main (geodynamo) field was calculated for an inaccurate location.

To address the contribution from the geodynamo, we use the IGRF model, version 11 [*Finlay et al*., 2010], which has coefficients specifying the time-varying field (the secular variation) through 2015. The calculation for the perturbations is

$$\delta \boldsymbol{B} = \boldsymbol{B}_{\mathrm{obs}} - \boldsymbol{B}_{\mathrm{IGRF}} \tag{2}$$

where $\mathbf{B}_{\mathrm{obs}}$ is the magnetic field vector observed by SSM, $\mathbf{B}_{\mathrm{IGRF}}$ is the magnetic field vector produced by the IGRF model for the spacecraft location and altitude, and $\delta\mathbf{B}$ is the magnetic perturbation vector. The subtraction is performed in the spacecraft coordinate frame, with the IGRF vector rotated into spacecraft frame from the geographic frame using the inverse of the transformation described in the previous section. A set of example perturbations from two F16 polar crossings in either hemisphere is shown in Figure 1a. Figure 1b shows the difference between the perturbations in Figure 1a, calculated using the new spacecraft locations, and the perturbations originally included in the MFR files. Figure 1c shows the amount by which the IGRF model field changes per 7 km along spacecraft track (7 km is the great-circle distance between two DMSP locations 1 s apart). This is included to provide context for Figure 1b and suggests that the recomputed locations may often be within 1 s (7 km) of the "operational" locations for these later DMSP spacecraft (which were GPS equipped). Statistics of the difference between original and recalculated locations are included in the supporting information.

3.2. Nuisance Signal Removal: Jumps

Contributions from the spacecraft itself are a more difficult issue. The body-mounted SSM instruments suffered from these to such an extent that they were not usable for the more subtle observations in their planned mission, such as monitoring the year-by-year secular variation of Earth's field [*Rich*, 1984].

Although more recent DMSP spacecraft mitigated this problem by moving the instrument 5 m away from the spacecraft using a telescopic boom, remnant fields from the spacecraft still influence the data. There are two main types of undesired field left after IGRF subtraction: instrument on-off jumps and the long period baseline.

On-off jumps are due to intermittently operating high-current equipment on the spacecraft. Examples include the heaters and the spacecraft attitude control system, which uses electric current through coils to create torques on the spacecraft using the earth's main field [*Rich*, 1984]. Their effects on the signal appear as a near-instantaneous change in the baseline of the magnetometer data, as the equipment turns on, which holds constant for tens of seconds to minutes and then drops back to the original baseline level when it turns off again. Fortunately, these jumps do not distort any of the FAC-induced fields while they are in effect because they simply represent a constant offset in the magnetic field value. To correct these jumps, we have developed an automatic algorithm inspired by the image-processing concept of edge detection, using the component of the perturbations along the Apex field-aligned direction (d3) to detect the jumps even in auroral regions, where the perturbations along other vector components may be very dynamic due to FACs. An in-depth description of this algorithm is beyond the scope of this paper, and it is not yet mature enough to allow us to run it unsupervised over the decades of spacecraft data we plan to release. However, we provide the algorithm implemented in Python at NOAA NCEI (see acknowledgements) and via this paper's permanent URL: http://www.purl.org/dmsp_ssm_level2), which corrects most jumps in the magnetic perturbations, saving the result to a new variable in any provided DMSP SSM CDF file.

3.3. Nuisance Signal Removal: Baseline

The second type of residual field that is not due to the FAC system is a slowly evolving, sinusoid-like variation in the baseline of the magnetometer data. *Rich et al.* [2007] describe this baseline variation and the remedy/characterization procedure we have chosen to implement for our Level-2 data. Interestingly, their study found that the value of the along-spacecraft-track (*Y* axis) component of the baseline at the magnetic equator is highly correlated with the *Dst* index, implying a ring current source. However, they also found that the baseline is not zero when the *Dst* is zero. In this case its magnitude is near constant. The magnitude of the zero-*Dst* baseline was found to differ from spacecraft to spacecraft. This indicates that the baseline is a combination of geophysical and instrumental effects. Examples of the later could include incomplete main field removal, imperfect magnetometer alignment, and imperfectly compensated thermal effects on the instrument and boom.

Their process for baseline estimation was historically called "MFIT" and consists of (1) dividing the data into polar region crossings; (2) then for each crossing, isolating the region free of FAC-induced fields; (3) fitting a polynomial to the baseline using only the FAC-free data; and (4) subtracting this polynomial from the perturbations. The "FAC-free" region is determined using the SSJ precipitating particles sensor. FACs typically only occur in, above, or very slightly below the auroral oval, a region which is characterized by near continuous particle precipitation. By determining when the higher energy (~1–30 keV) electron precipitation measured by SSJ drops below a threshold, we determine the position and extent of the auroral region (see section 4 for more details). To be conservative, the MFIT procedure sets its latitude boundary a few degrees below the equatorward edge of the auroral region. Equatorward of this latitude we consider the magnetometer observations FAC-free polynomials are then fit to each component of the magnetometer data (fifth degree for *X* and *Z* and seventh degree for *Y*). Figure 1d plots the polynomial fits for the *X*, *Y*, and *Z* perturbations for two polar crossings made by F16 on 29 May 2010 (during a geomagnetic storm). The grey shading indicates the regions in and poleward of the aurora in which FAC-induced perturbations are expected and thus are not used in the fit. Comparison with Figure 1a shows the amplitude of the baseline is noticeable, even during these fairly geomagnetically active ($Kp = 4$) conditions.

3.4. Uncertainty in the SSM Observations

Quantifying the reliability of space-based observations is a challenge, and magnetometer data are no exception. A systematic approach [*Alken et al.,* 2014] is to first attempt to correct known sources of uncertainty (e.g., core misalignment/nonorthogonality, scalar offset, and time slips) by calibrating the magnetometer observations against Pomme-8, a high-order model of the main field [*Lühr and Maus*, 2010]. Pomme-8 also includes an external field component (i.e., it models magnetic perturbations due to geomagnetic activity), meaning

the model also captures the *Dst*-correlated portion of the magnetometer signal that we address with MFIT (section 3.3). Their calibration reduced the average residuals between DMSP F16 measured magnetic field and Pomme-8 model field from ~80 nT to ~10 nT [e.g., *Alken et al*., 2014, Figures 6 and 7]. *Knipp et al.* [2014] directly compared DMSP SSM magnetic perturbations in Apex coordinates with those from the Active Magnetosphere and Planetary Electrodynamics Response Experiment (AMPERE) project by searching for "magnetic conjunctions," and *Knipp et al.* [2015] applied this technique again to compare DMSP perturbations with those of the NASA Space Technology 5 (ST5) three-spacecraft mission, finding a median perturbation discrepancy of $<$50 nT for $Kp < 2$. These studies suggest instrument uncertainties in the range of 50–70 nT. Considering Figure 1c, this is comparable to the change in the main field from one spacecraft location to the next at 1 s cadence. This order of uncertainty, in the range of 50–70 nT, may be realistically the best that can be done by starting with quasi-second cadence data as we do, considering that each 1 s SSM observation available in the MFR files is in fact an average across 7 km, over which the main field is likely changing as in Figure 1c, and spacecraft currents may also be in play.

3.5. Comparisons With Other DMSP SSM Data Sets

To demonstrate differences between our data and other SSM data sets currently available, we have compared our magnetic perturbations, cleaned of undesired signals as shown in the previous subsections, with unprocessed magnetic perturbation data from other sources. Original SSM observations are available from and the Madrigal database (as curated by Boston College) and NOAA NCEI (see section 2). Our methodology focuses on getting the best estimate of high-latitude FAC related perturbations, assuming that perturbations are nearly zero at the equator as part of the MFIT process (section 3.3). This is the major difference apparent from the comparison. The perturbations from our data set are near zero near the equator, while those of the original data sets vary with the *Dst* (as demonstrated in *Burke et al.* [2011] and *Rich et al.* [2007]). For users who wish to examine original SSM measurements, our new data set discussed herein also contains these original uncorrected perturbations. Detailed methodology of this comparison, along with graphics, are available in the supporting information.

3.6. Data Access

Level-2 SSM data are available through and synchronized between the National Oceanic and Atmospheric Administration (NOAA) National Centers for Environmental Information (NCEI), http://www.ngdc.noaa.gov/stp/satellite/dmsp/ and the National Aeronautical and Space Administration (NASA) Space Physics Data Facility (SPDF) Coordinated Data Analysis Web (CDAWeb) http://cdaweb.gsfc.nasa.gov/istp_public/. Data are currently available in NASA CDF format for F16-F18, 2010–2014, and we plan to process SSM for these spacecraft through to the present (or the end of their lifetimes). The following PURL (an archival web address for publications) http://www.purl.org/dmsp_ssm_level2 will redirect to the most current code and documentation associated with this paper. Documentation and software are also available through the NOAA NCEI portal. Additional information on the files is tabulated in the supporting information.

4. Auroral Boundaries

Our magnetometer reprocessing effort coincided with a similar reprocessing of data from the SSJ precipitating electrons and ion instrument [*Redmon et al*., 2017]. Using the SSJ5 electron precipitation measurements from DMSP F16, F17, and F18 we implemented an improved version of the *Redmon et al.* [2010] auroral boundary identification algorithm. This algorithm finds the portion of DMSP orbits in which the spacecraft was passing through the aurora. This information is traditionally recorded as the magnetic latitude and local time at which the spacecraft entered and left the aurora, the auroral boundaries. The intent of this additional work in the context of our magnetometer reprocessing was to provide a dynamic auroral context for the magnetic perturbations. That is, when possible, we classify the auroral region of each SSM observation (i.e., poleward, equatorward, and inside), according to our definition of auroral electron precipitation (see next section). We anticipate that classifying each magnetic perturbation datum by auroral region will enable future work on characterizing field-aligned current signatures and effects, e.g., of subauroral polarization streams (SAPS) and the cusp/polar cap.

Our scheme begins by assuming that any particular DMSP spacecraft transit the auroral oval twice per northern or southern polar region crossing, once on the morningside of the aurora and once on the

eveningside. For simplicity we will refer to each such half orbit, starting at the magnetic equator on one side, extending over the northern or southern pole and ending at the equator on the other side, as a "polar pass." It is important to note that due to the offset of Earth's magnetic poles Earth's rotational axis, the roughly dawn-dusk spacecraft tracks oscillate slightly in magnetic local time over the course of the day, meaning that the spacecraft does not always intersect the aurora twice, instead "grazing" the aurora and never exiting into the polar cap (see orbit example in Figure 1 of *Rastätter et al.* [2016]). In this case the above assumption is violated and the pass is recorded as "no boundary identified." We only use polar passes in which all four auroral boundaries are clearly identified.

Identifying the electron precipitation aurora begins by dividing each spacecraft day of data into individual polar passes. Next, we integrate the electron energy flux from the higher energy SSJ channels with respect to particle kinetic energy using the technique devised in *Hardy et al.* [1985]. This gives us, J_E, the total energy flux of electrons with kinetic energy between 1.3 keV and 30 keV (in units of eV/cm^2/s/sr). Dropouts in the high-energy electron precipitation lasting a few seconds or more are common in the aurora as measured by SSJ (e.g., polar cap arcs). To ensure that we identify the main auroral oval, we perform a 15 s boxcar average of the flux which prevents dropouts from dissecting the auroral region. The next step is to identify candidate auroral regions, two of which will then be chosen as morningside and eveningside portions of the aurora. The candidate regions are those portions of the polar pass where the SSJ instrument recorded energy flux J_E continuously above a threshold $J_{E,\max}$. A typical polar pass intersects between 2 and 5 such regions, and a typical region spans 5–15° magnetic latitude. We chose the threshold $J_{E,\max}$ to be 10^9 eV/cm^2/s/sr after by-hand analysis of ~60 polar passes from a range of dates, picking a $J_{E,\max}$ value which produced auroral regions which had SSJ electron spectra consistent with a source region of the central or boundary plasma sheet as described by *Newell et al.* [1996].

After identifying all of the auroral region candidates, we can determine which pair is most likely to be the aurora. For each possible pair (m, n), we rate the likelihood of both members being crossings of the aurora (as opposed to one being an isolated arc, for example) using a figure of merit (FOM). The formula for the FOM for candidate pair (m, n) is shown in equation (3):

$$\mathrm{FOM}(m,n) = \frac{(A_m + A_n)}{A_{\mathrm{Max}}} + \left(1 - \frac{\sigma A_m}{A_m}\right) + \left(1 - \frac{\sigma A_n}{A_n}\right) + \frac{t_{m,n}}{20\times 60} \tag{3}$$

where A is the total summed energy flux J_E encompassed by the region in question, $A_{\max}$ is the largest such value amongst all regions in the polar pass, $t_{m,n}$ is the polar cap width in seconds (the amount of spacecraft flight time between the end of the first region (m) and the beginning of the second (n)), and $\frac{\sigma A}{A}$ is the average relative uncertainty of the energy flux of a particular region. The uncertainty metric is new to this study and reduces the FOM when considering regions in which the uncertainty in the energy flux is high because of low instrument counts. This prevents, among other problems, misidentification of radiation belt proton contamination as auroral precipitation. It is calculated by summing the uncertainty values ($\sigma J_E(t)$) associated with each energy flux observation (i.e. $J_E(t) \pm \sigma J_E(t)$) encompassed by the region and then dividing by A, producing an average relative uncertainty. The uncertainties $\sigma J_E(t)$ are those included with the new SSJ data set and are detailed in *Redmon et al.* [2017].

Each value in the FOM is normalized, so that FOMs of different polar passes can be compared. The first term is normalized by the largest total region energy flux for the polar pass ($A_{\max}$), and the uncertainty terms are limited by constraining $\frac{\sigma A}{A}$ to 1 on the rare occasion that it exceeds unity. The polar cap width is normalized to 20 min, which is a typical polar cap crossing time. An application of these FOMs is to quickly filter the highest-quality auroral identifications. We have found that a FOM of 3 is a safe lower boundary.

Once the FOMs have been determined, the final boundary identification can be made. The pair of candidate auroral regions with the highest FOM "win" and are designated the morningside and eveningside aurora. The auroral boundaries are thus the beginning and end of their respective auroral region, and the polar cap is the area between the highest latitude edges of the two auroral regions. Note that this technique allows asymmetric auroral shapes, with, for example, the morningside wider in latitude than the eveningside.

Figure 2 shows an example boundary determination. Each green shaded region (numbered 0–3) represents an auroral zone candidate, i.e., a region of continuously above-threshold flux. The FOMs are computed for

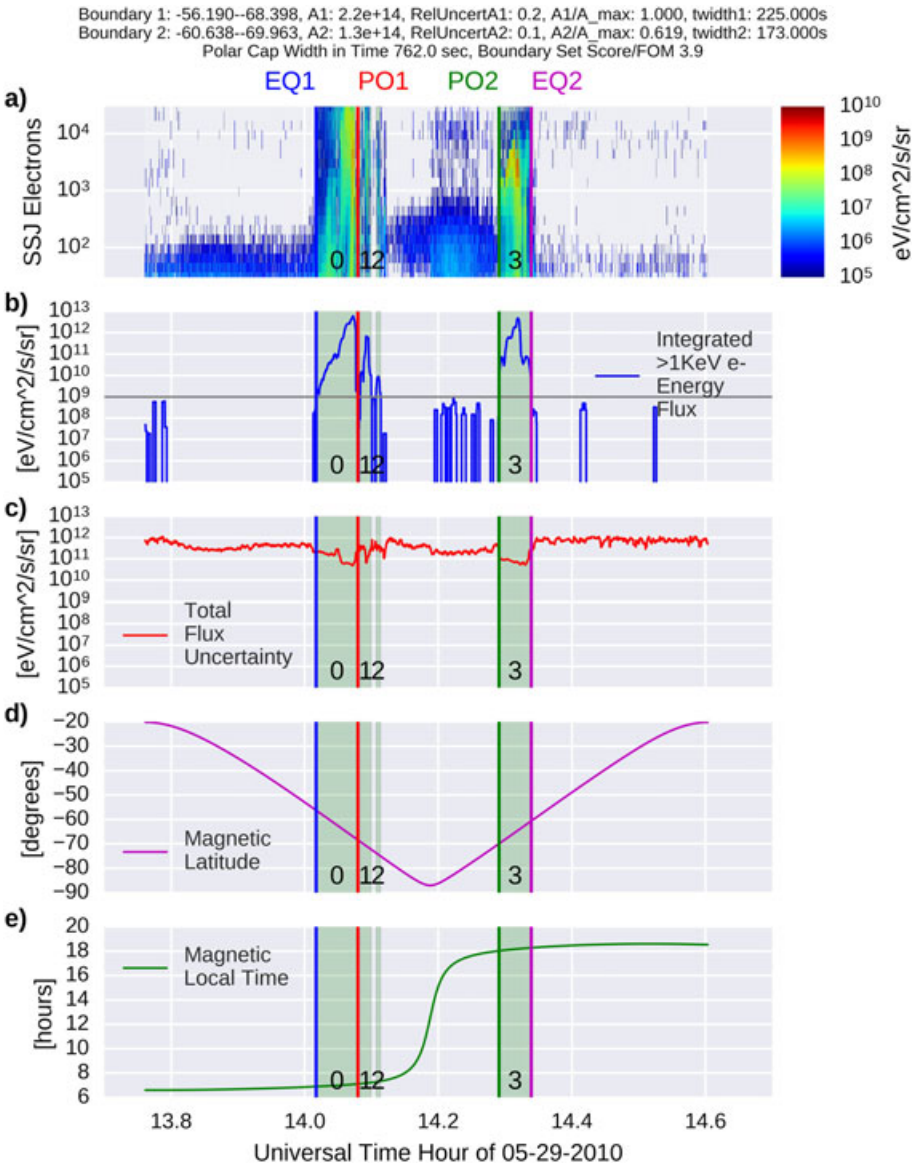

Figure 2. Example Southern Hemisphere boundary identification from DMSP F16 on 29 May 2010. This figure shows the DMSP SSJ electron precipitation data from one southern polar region crossing. (a) The electron energy spectrogram with the channel energy of the 19 DMSP SSJ channels on the *y* axis and time on the *x* axis. (b) The electron energy flux, integrated over all of the channels with center energies >1 keV, and the grey horizontal line shows our threshold for boundary detection. There are four auroral region candidates shown shaded in green and labeled 0–3. The final boundary determination bounds the pair of auroral region candidates found to produce the highest FOM (0 and 3) and is shown as thick vertical lines, with the codes EQ for equatorward boundaries and PO for poleward boundaries. Metrics about the boundary identification (the inputs to the score/figure of merit equation (3) and the resulting FOM) are shown in the figure title. (c) The uncertainty in total electron energy flux σJ_E, which is summed across region m to produce σA_m, which is considered in the FOM. (d and e) The spacecraft location as Apex magnetic latitude and magnetic local time.

each pair with one region on either side of the highest latitude (either side of the magnetic pole). In this case the only pairs that were considered are (1, 3), scoring 2.71, and (0, 3), scoring 3.87. Region 2 was disqualified from consideration because it was too short (<30 seconds of data). Thus, (0, 3) wins, meaning 0 and 3 are designated the dawn-and-duskside auroral crossings, and the poleward and equatorward edges of each are the boundaries for this pass. The auroral boundary algorithm is run on all days of data in the SSM data set as part of the creation process and is included in the SSM CDF files as the variable "AURORAL_REGION." AURORAL_REGION has a value for each SSM observation and is categorical, with 0 indicating no boundary determined for that pass, 1 indicating the spacecraft was subauroral, 2 indicating the auroral zone, and 3,

the polar cap. The FOM is also stored in the SSM CDF in a similar variable called AURORAL_BOUNDARY_FOM to facilitate locating the best boundary identifications. Comma-separated-variable (CSV) files which specify the time and location of these auroral boundaries by date and spacecraft are also generated and available by request.

To summarize the auroral boundary technique in comparison to its progenitor, we emulate *Redmon et al.* [2010] in that our auroral region is defined as a region with >1 keV electron energy flux continuously above an experimentally-determined threshold. However, the threshold value differs from that of the original study, because Redmon et al. used data from DMSP F12 and F13 which carried the SSJ4 instrument, and we have used the SSJ5-equipped F16, F17, and F18. Our algorithm also differs from the *Redmon et al.* [2010] technique in that we consider the uncertainties in the SSJ flux measurements, which are an innovation of the reprocessing of SSJ data detailed in the companion paper *Redmon et al*. [2017].

5. Field-Aligned Currents (FAC)

The FAC density encountered by a single spacecraft can be estimated using in situ magnetic perturbation data. After SSM data processing is complete, we get reasonable estimates of the FAC densities at several scale sizes. Here we describe our methodology for determining large-scale FACs (those with scale sizes at 110 km altitude >300 km), using the Minimum Variance Analysis (MVA) technique [*Sonnerup and Scheible*, 1998]. This technique differs from the technique traditionally used for DMSP, that of *Higuchi and Ohtani* [2000]. We chose MVA instead of the traditional technique because we are also interested in examining mesoscale currents [e.g., as was done for NASA Space Technology 5 in *Le et al.* [2009]]. The *Higuchi and Ohtani* [2000] technique is focused primarily on large-scale FACs. The analysis of the FACs from DMSP SSM with scale sizes <300 km and their spatial distribution in dynamic boundary coordinates are the subject of a future study. We briefly compare our results with results based on the traditional technique in the final section of this paper, with good agreement.

To isolate the portion of the perturbations due to the large-scale FAC, each polar crossing of DMSP SSM perturbations is filtered with a digital sixth order Butterworth low-pass filter with a critical frequency of 45 s, corresponding to about 300 km at 110 km altitude. Then, the polar region crossing is divided into two halves at the highest latitude point in the orbit, and MVA is performed separately on each half, considering all data from that half of the pass as one "sample." If we make the assumption that each half of the polar pass represents the spacecraft crossing a number of parallel current sheets, we can consider the MVA basis (i, j, k) to be statistically current sheet aligned. We can then rotate the perturbations from the spacecraft coordinate frame to (i, j, k) and approximate Ampere's Law with equation (4) to determine the FAC density.

$$j_k = \frac{1}{\mu_0 \Delta t} \frac{\Delta B_j}{v \sin(\phi)} \tag{4}$$

where Δt represents the change in time and ΔB_j the change in the component of the magnetic field perpendicular to the current sheet between two subsequent 1 s SSM observations, v is the spacecraft speed, and ϕ is the angle between the spacecraft velocity direction (the SSM + Y direction) and the i direction (the "attack angle"). Although *Lühr et al*. [2015] showed using SWARM measurements that the actual longitudinal extent of current sheets compared to their latitudinal extent is typically 4:1 on the nightside, *Lühr et al*. [1996] have shown that the infinite sheet assumption implicit in this method never overestimates the FAC density. Therefore, we can still study the locations and, to some extent, the relative intensities of current systems in different regions with confidence that we are not "making up" currents where none exist.

6. Large-Scale Field-Aligned Current Locations Relative to Auroral Boundaries

To demonstrate the utility of the SSM data, including the in situ auroral boundaries, we have again followed the method of *Redmon et al.* [2010] and re-expressed our FACs in dynamic auroral boundary coordinates. Auroral boundary coordinates replace the latitude of a measurement with its distance from the closest auroral boundary [see also *Andersson et al.*, 2004; *Peterson et al*., 2008]. Equations (5)–(7) show the conversion from latitude to auroral boundary latitude for these quantities in the cases of measurements in the polar cap, the auroral zone, and below the equatorward auroral boundary.

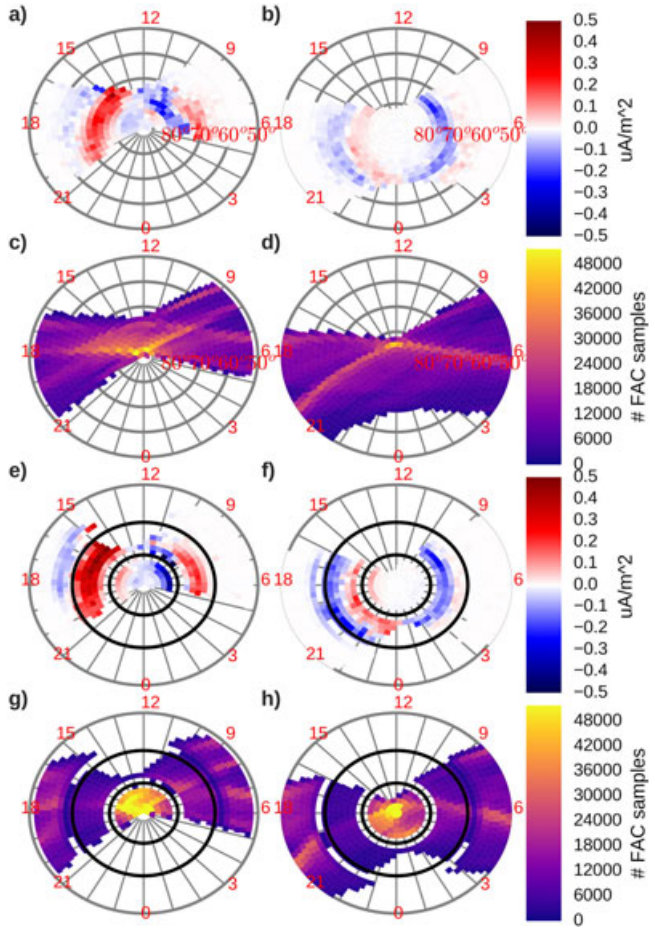

Figure 3. Large-scale FACs in magnetic and auroral boundary coordinates. The statistical results for northern summer (±45 days around June solstice) SSM FAC density from DMSP F16, F17, and F18 for 2010–2012 are binned in equal-area bins. Northern Hemisphere data are on the left, while the southern data are on the right. (a and b) Northern and southern bin-average FAC in magnetic Apex coordinates; (c and d) the number of samples per bin for the same. (e and f) The same FAC data but binned relative to the associated in situ auroral boundary from DMSP SSJ, with the black circles representing the equatorward and poleward auroral boundaries. (g and h) Counts per bin are significantly rearranged when the data are binned in boundary coordinates. Bins with fewer than 2000 observations are removed for more reliable results.

$$L_{PO}(\lambda) = \frac{|\lambda - \lambda_{PO}|}{90 - |\lambda|}, \quad \lambda > \lambda_{PO} \qquad (5)$$

$$L_{AZ}(\lambda) = \frac{|\lambda - \lambda_{EQ}|}{|\lambda_{PO} - \lambda_{EQ}|}, \lambda_{EQ} < \lambda < \lambda_{PO} \qquad (6)$$

$$L_{EQ}(\lambda) = \frac{|\lambda - \lambda_{EQ}|}{|\lambda_{EQ}|}, \quad \lambda < \lambda_{EQ} \qquad (7)$$

where λ is latitude and EQ is the equatorward edge of the auroral boundary (the lowest latitude with above-threshold electron energy flux) and PO is the poleward edge of the auroral boundary (the highest latitude with above-threshold electron energy flux). For any particular polar pass, the transformation can only be performed if algorithm of section 4 identified both morningside and eveningside auroral crossings. If the spacecraft did not exit into the polar cap, for example, we exclude that pass from future consideration.

We have performed this transformation for a selection (± 45 days about northern summer (June) solstice and only passes with a boundary identified) of the data from 2010 to 2012, including measurements from F16, F17, and F18 with the results shown in Figure 3. For comparison, the data have been binned first in equal-area polar-coordinate bins with the Apex magnetic colatitude as radial coordinate and the magnetic local time as the azimuth (Figures 3a and 3b). The center of the polar plot is the northern or southern magnetic pole for the left or right column of graphics, respectively. Because the subset chosen for this graphic is northern summer, the Northern Hemisphere FACs are notably stronger, as it is tilted into the solar wind, allowing more opportunities for flank and lobe merging, and the solar-induced conductivity is higher. The cusp, or region-0 current system, is visible in the Northern Hemisphere but is not clearly featured in the Southern Hemisphere. Beyond this, the two hemispheres reproduce the standard region-1 and region-2 patterns. There is an apparent strength discrepancy between dawn and dusk side current systems which may have some physical aspect, but is more likely simply a geometric effect of the orbits causing the MVA-based FAC technique to systematically underestimate the currents on one side of the polar cap versus the other. When the data are transformed into dynamic auroral boundary coordinates (Figures 3e and 3f), additional characteristics of the data emerge. The first immediate difference is the dawn-dusk asymmetry where the R1 and R2 systems lie relative to the boundary. One thing that is not obvious from the plots is that the dawnside auroral region as determined by electron precipitation is consistently wider (covers a larger Apex latitude range) than the duskside. Also, the degree of asymmetry is different in the Northern versus Southern Hemisphere. In the special case of the nightside, this dawn-dusk asymmetry in R1 and R2 locations relative to the auroral

boundary has been noted by *Ohtani et al.* [2010], using a different set of auroral boundaries [*Newell et al.*, 1996] and the *Higuchi and Ohtani* [2000] FAC algorithm. Our interpretation of the source of the phenomena has to do with the current carriers of the FACs. The duskside R2 current has a downward sense and is thus carried either by downward ions, or by upward electrons, the latter of which DMSP SSJ cannot observe because it only senses particles with pitch-angles near the loss cone. Thus, it is very possible for there to be sufficient current carries for the downward FAC below the boundary of strong electron precipitation. For the dawnside, however, this is not the case. The upward R2 FAC must be carried by either electron precipitation or upward ions, the latter of which are generally not numerous enough to carry current. Therefore, R2 usually appears above the equatorward boundary, i.e., in the region of strong electron flux.

7. Summary

The DMSP SSM data for F16, F17, and F18 from 2010–2014 have been reprocessed and are available through NASA CDAWeb and through NOAA NCEI. The reprocessing includes updated spacecraft locations, which were used to recompute magnetic perturbations using IGRF-11. Spacecraft locations are provided in both geographic and magnetic Apex coordinate systems. Vector magnetic perturbations are provided in spacecraft body-fixed, geographic east-north-up, and Apex main field-aligned reference frames. Coincident DMSP SSJ5 electron precipitation data were used to find in situ auroral boundaries, in an improvement on the *Redmon et al.* [2010] algorithm. The resulting information is embedded into the magnetometer data set by classifying each measurement as subauroral, auroral, polar cap, or unknown (no boundary found). The new magnetic perturbations can be used to compute large-scale field-aligned currents that reproduce documented asymmetries in the dawn-dusk region-2 FAC locations relative to electron precipitation auroral boundaries.

Acknowledgments

We would like to thank all of our Department of Defense collaborators, without whom we would not have been able to perform this work. These include Fred Rich (MITLL, AFRL retired), Daniel Ober, and Gordon Wilson (AFRL). We would also like to thank Kevin Martin and Patricia Doherty (Boston College), and Robert McGuire and Tamara Kovalik (NASA). DMSP SSM data for the comparison in section 8 were downloaded for the CEDAR Madrigal Database: http://cedar.openmadrigal.org/. Madrigal database operations and DMSP SSM processing at Boston College are supported by Millstone Hill Geospace Facility activities under cooperative agreement AGS-1242204 between the National Science Foundation and the Massachusetts Institute of Technology. The project described herein was partially funded by NASA grant NNX13AG07G. D.J. Knipp and L.M. Kilcommons were partially supported by NSF Polar Programs grant 1443703 and by AFOSR award FA9550-16-1-0364. The data set described herein is available from NASA SPDF CDAWeb (http://cdaweb.gsfc.nasa.gov/istp_public/) and from NOAA NCEI (http://www.ngdc.noaa.gov/stp/satellite/dmsp/), along with further documentation and associated software. The following PURL http://www.purl.org/dmsp_ssm_level2 also points to the code and documentation associated with this paper. The NCAR High Altitude Observatory is supported by the National Science Foundation.

References

Alken, P., S. Maus, H. Lühr, R. J. Redmon, F. Rich, B. Bowman, and S. M. O'Malley (2014), Geomagnetic main field modeling with DMSP, *J. Geophys. Res. Space Physics*, *119*, 4010–4025, doi:10.1002/2013JA019754.

Andersson, L., W. K. Peterson, and K. M. McBryde (2004), Dynamic coordinates for auroral ion outflow, *J. Geophys. Res.*, *109*, A08201, doi:10.1029/2004JA010424.

Baker, K. B., and S. Wing (1989), A new magnetic coordinate system for conjugate studies at high latitudes, *J. Geophys. Res.*, *94*(A7), 9139–9143, doi:10.1029/JA094iA07p09139.

Burke, W. J., G. R. Wilson, C. S. Lin, F. J. Rich, J. O. Wise, and M. P. Hagan (2011), Estimating *Dst* indices and exospheric temperatures from equatorial magnetic fields measured by DMSP satellites, *J. Geophys. Res.*, *116*, A01205, doi:10.1029/2010JA015310.

Chornay, D. J. (1987), Operations handbook for DMSP/SSM magnetometer, NASA/GSFC laboratory for extraterrestrial physics. [Available at http://satdat.ngdc.noaa.gov/dmsp/docs/NASA%20-%201987%20-%20SSM%20Design%20and%20Operation.pdf.]

Finlay, C. C., et al. (2010), International Geomagnetic Reference Field: The eleventh generation, *Geophys. J. Int.*, *183*(3), 1216–1230, doi:10.1111/j.1365-246X.2010.04804.x.

Hall, R. C. (2001), A history of the military polar orbiting meteorological satellite program, Office of the Historian, National Reconnaissance Office. [Available at http://www.nro.gov/history/csnr/programs/docs/prog-hist-02.pdf.]

Hardy, D. (1984), Precipitating electron and ion detectors (SSJ/4) for the block 5D/flights 6-10 DMSP satellites: Calibration and data presentation, Rep AFGL-TR-84-0317.

Hardy, D. A., M. S. Gussenhoven, and E. Holeman (1985), A statistical model of auroral electron precipitation, *J. Geophys. Res.*, *90*(A5), 4229–4248, doi:10.1029/JA090iA05p04229.

Higuchi, T., and S. Ohtani (2000), Automatic identification of large-scale field-aligned current structures, *J. Geophys. Res.*, *105*(A11), 25305–25315, doi:10.1029/2000JA900073.

Knipp, D. J., T. Matsuo, L. Kilcommons, A. Richmond, B. Anderson, H. Korth, R. Redmon, B. Mero, and N. Parrish (2014), Comparison of magnetic perturbation data from LEO satellite constellations: Statistics of DMSP and AMPERE, *Space Weather*, *12*, 2–23, doi:10.1002/2013SW000987.

Knipp, D. J., L. M. Kilcommons, J. Gjerloev, R. J. Redmon, J. Slavin, and G. Le (2015), A large-scale view of Space Technology 5 magnetometer response to solar wind drivers, *Earth Space Sci.*, *2*(4), 115–124, doi:10.1002/2014EA000057.

Le, G., Y. Wang, J. A. Slavin, and R. J. Strangeway (2009), Space Technology 5 multipoint observations of temporal and spatial variability of field-aligned currents, *J. Geophys. Res.*, *114*, A08206, doi:10.1029/2009JA014081.

Lühr, H., and S. Maus (2010), Solar cycle dependence of quiet-time magnetospheric currents and a model of their near-Earth magnetic fields, *Earth Planets Space*, *62*(10), 843–848, doi:10.5047/eps.2010.07.012.

Lühr, H., J. F. Warnecke, and M. K. A. Rother (1996), An algorithm for estimating field-aligned currents from single spacecraft magnetic field measurements: A diagnostic tool applied to Freja satellite data, *IEEE Trans. Geosci. Remote Sens.*, *34*(6), 1369–1376, doi:10.1109/36.544560.

Lühr, H., J. Park, J. W. Gjerloev, J. Rauberg, I. Michaelis, J. M. G. Merayo, and P. Brauer (2015), Field-aligned currents' scale analysis performed with the Swarm constellation, *Geophys. Res. Lett.*, *42*, 1–8, doi:10.1002/2014GL062453.

Mathews, G. J., and S. S. Towheed (1995), NSSDC OMNIWeb: The first space physics WWW-based data browsing and retrieval system, *Comput. Netw. ISDN Syst.*, *27*(6), 801–808, doi:10.1016/0169-7552(95)00033-4.

Matsuo, T., D. J. Knipp, A. D. Richmond, L. Kilcommons, and B. J. Anderson (2015), Inverse procedure for high-latitude ionospheric electrodynamics: Analysis of satellite-borne magnetometer data, *J. Geophys. Res. Space Physics*, *120*, 5241–5251, doi:10.1002/2014JA020565.

Maus, S., et al. (2005), The 10th generation international geomagnetic reference field, *Phys. Earth Planet. In.*, *151*(3–4), 320–322, doi:10.1016/j.pepi.2005.03.006.

Miller, Neil I. and L. E. Sexton (2001), Observations and calibrations of DMSP F15 SSM data December 1999–October 2000, Radex Inc, Bedford, Mass, January 10, 2001. [Available at http://www.dtic.mil/cgi-bin/GetTRDoc?Location=U2&doc=GetTRDoc.pdf&AD=ADA419157.]

Newell, P. T., Y. I. Feldstein, Y. I. Galperin, and C.-I. Meng (1996), Morphology of nightside precipitation, *J. Geophys. Res.*, *101*(A5), 10,737–10,748, doi:10.1029/95JA03516.

Ohtani, S., S. Wing, P. T. Newell, and T. Higuchi (2010), Locations of night-side precipitation boundaries relative to R2 and R1 currents, *J. Geophys. Res.*, *115*, A10233, doi:10.1029/2010JA015444.

Peterson, W. K., L. Andersson, B. C. Callahan, H. L. Collin, J. D. Scudder, and A. W. Yau (2008), Solar-minimum quiet time ion energization and outflow in dynamic boundary related coordinates, *J. Geophys. Res.*, *113*, A07222, doi:10.1029/2008JA013059.

Rastätter, L., et al. (2016), GEM-CEDAR challenge: Poynting flux at DMSP and modeled joule heat, *Space Weather*, *14*, 113–135, doi:10.1002/2015SW001238.

Redmon, R. J., W. K. Peterson, L. Andersson, E. A. Kihn, W. F. Denig, M. Hairston, and R. Coley (2010), Vertical thermal O^+ flows at 850 km in dynamic auroral boundary coordinates, *J. Geophys. Res.*, *115*, A00J08, doi:10.1029/2010JA015589.

Redmon, R. J., L. M. Kilcommons, and D. J. Knipp (2017), New DMSP database of precipitating electrons and ions, *J. Geophys. Res. Space Physics*, doi:10.1002/2016JA023339.

Rich, F. J. (1984), Fluxgate magnetometer (SSM) for the Defense Meteorological Satellite Program (DMSP) block 5D-2, Flight 7. [Available at http://www.dtic.mil/cgi-bin/GetTRDoc?Location=U2&doc=GetTRDoc.pdf&AD=ADA155229.]

Rich, F. J., J. M. Bono, W. J. Burke, and L. C. Gentile (2007), A space-based proxy for the *Dst* index, *J. Geophys. Res.*, *112*, A05211, doi:10.1029/2005JA011586.

Richmond, A. D. (1992), Assimilative mapping of ionospheric electrodynamics, *Adv. Space Res.*, *12*(6), 59–68, doi:10.1016/0273-1177(92)90040-5.

Richmond, A. D. (1995), Ionospheric electrodynamics using magnetic Apex coordinates, *J. Geomag. Geoelec.*, *47*(2), 191–212, doi:10.5636/jgg.47.191.

Richmond, A. D., E. C. Ridley, and R. G. Roble (1992), A thermosphere/ionosphere general circulation model with coupled electrodynamics, *Geophys. Res. Lett.*, *19*(6), 601–604, doi:10.1029/92GL00401.

Sonnerup, B. U. Ö., and M. Scheible (1998), Minimum and maximum variance analysis, *ISSI Scientific Rep. Ser.*, *1*, 185–220.